Time-dependent density-functional theory of strong-field ionization of atoms by soft x rays

A. Crawford-Uranga,[1,*] U. De Giovannini,[1] E. Räsänen,[2] M. J. T. Oliveira,[3] D. J. Mowbray,[1] G. M. Nikolopoulos,[4]
E. T. Karamatskos,[5,†] D. Markellos,[5] P. Lambropoulos,[4,5] S. Kurth,[1,6] and A. Rubio[1,‡]

[1]*Nano-Bio Spectroscopy Group and ETSF Scientific Development Center, Departamento de Física de Materiales, Centro de Física de
Materiales CSIC-MPC and DIPC, Universidad del País Vasco UPV/EHU, Avenida de Tolosa 72, E-20018, San Sebastián, Spain*
[2]*Department of Physics, Tampere University of Technology, FI-33101 Tampere, Finland*
[3]*Center for Computational Physics, University of Coimbra, Rua Larga, 3004-516 Coimbra, Portugal*
[4]*Institute of Electronic Structure and Laser, FORTH, P.O. Box 1527, GR-71110 Heraklion, Greece*
[5]*Department of Physics, University of Crete, P.O. Box 2208, GR-71003 Heraklion, Crete, Greece*
[6]*IKERBASQUE, Basque Foundation for Science, E-48011, Bilbao, Spain*

We demonstrate the capabilities of time-dependent density functional theory (TDDFT) for strong-field, short-wavelength (soft x-ray) physics, as compared to a formalism based on rate equations. We find that TDDFT provides a very good description of the total and individual ionization yields for Ne and Ar atoms exposed to strong laser pulses. We assess the reliability of different adiabatic density functionals and conclude that an accurate description of long-range interactions by the exchange and correlation potential is crucial for obtaining the correct ionization yield over a wide range of intensities (from 10^{13} to 5×10^{15} W/cm^2). Our TDDFT calculations disentangle the contribution from each ionization channel based on the Kohn-Sham wave functions.

PACS number(s): 32.80.Rm, 32.80.Fb, 31.15.ee, 42.55.Vc

I. INTRODUCTION

Recent advances in the development of free-electron lasers (FELs) have led to the generation of intense, ultrashort-duration, and short-wavelength radiation sources ranging from extreme ultraviolet (XUV) to hard x rays [1,2]. The possible applications encompass a broad area of topics, such as basic atomic and molecular physics, dense matter, and imaging of complex biomolecules, to mention only a few [3,4]. Because radiation in this wavelength range can ionize deep inner electrons, multiple ionization processes are an inevitable outcome. Understanding the mechanism underlying these processes [5–11] is of fundamental importance to this broad interdisciplinary field.

For infrared to optical high-intensity lasers, even for ultra-short pulse durations down to a few cycles, the validity of the single active electron (SAE) approximation is well established [12]. As a consequence, multiple ionization is dominated by sequential stripping of valence electrons. To the extent that for sufficiently high peak intensities, with ponderomotive energy much larger than the photon energy and Keldysh parameter $\gamma \ll 1$, nonsequential two- or three-electron escape may be observable, the recollision mechanism has been shown to provide a valid description [12]. However, even for intense long-wavelength radiation, it is still difficult to produce highly charged ions.

For infrared to optical high-intensity lasers, even for ultrashort pulse durations down to a few field cycles [12], the validity of the single active electron (SAE) approximation is well established [12]. Here, multiple ionization is dominated by sequential stripping of electrons [12]. For sufficiently high

laser intensities, where the ponderomotive energy is much larger than the photon energy and the Keldysh parameter is $\gamma \ll 1$, nonsequential two- or three-electron escape processes are also possible [12]. In this case, the recollision mechanism has been shown to provide a valid description. However, even for intense long-wavelength radiation it is still difficult to produce highly charged ions.

On the other hand, short-wavelength FEL radiation, more often than not, produces highly charged ions in abundance [5–9,13]. Typically, the stripping begins with the ejection of one or more subvalence electrons, but the physical processes that determine the course of events depend strongly on the photon energy range. For hard x rays, say above 2 keV, it is mainly single-photon inner shell electron ejections, followed by avalanches of Auger decays and rearrangement, that dominate. By the time highly ionized species appear, with ionization potentials higher than the photon energies, the pulse is essentially over, which minimizes the possibility of two- or multiphoton ionization [13]. However, for soft x-ray energies, say up to 300 eV or so, the single-photon subvalence ionization eventually mingles, with (nonlinear) multiphoton processes providing thus an unusual and theoretically demanding interplay between linear and nonlinear processes. For currently accessible FEL peak intensities for which the ponderomotive energy is much smaller than the photon energy, consistent with $\gamma \gg 1$, and for pulse durations of hundreds of field cycles, the lowest nonvanishing order perturbation theory (LOPT) in terms of rate equations and multiphoton cross sections, is a valid model [8] in the entire FEL photon energy range.

Although sequential ionization still plays a dominant role, an entirely different nonsequential mechanism of multiple ionization comes into play. The SAE and recollision-based models are totally inapplicable in this context, because sequential ionization begins with subvalence electrons, for which the relevant cross sections, be they single- or multiphoton, involve inter- as well as intra-shell correlations. Additionally, even within LOPT, the calculation of multiphoton cross sections,

*alisonc1986@gmail.com
†Present address: Institut für Laser-Physik, Universität Hamburg, Luruper Chaussee 149, D-22761 Hamburg, Germany.
‡angel.rubio@ehu.es

which requires explicit or implicit summations over complete sets of intermediate states, poses a formidable computational challenge; not to mention the further complexity introduced by the possibility of multiphoton multielectron escape [9,10]. Experimentation with alternative methods, circumventing this task, is therefore highly desirable.

Because FEL intensities are expected to increase and pulse durations to be shortened, LOPT is expected to lose its validity. In the soft x-ray regime, this is apt to occur for peak intensities above 10^{17} W/cm^2 and pulse durations well below 5 fs, at which point a nonperturbative approach will become necessary. Since solving the time-dependent Schrodinger equation beyond the SAE approximation is a daunting task even for two electrons [14,15], time-dependent density-functional theory (TDDFT) appears to be one of the few available options. Since this represents uncharted territory, we have chosen to assess the potential of the method by applying TDDFT to the calculation of total ionization, as well as individual ionic yields for Ne and Ar, under photon energies 93 and 105 eV, respectively. In both cases, we have chosen peak intensities for which LOPT is demonstrably valid, in addition to the availability of some experimental data [11,16]. We are thus in the position to obtain an assessment of the potential of TDDFT, before venturing into the nonperturbative regime.

Applications of TDDFT in the long-wavelength strong-field regime are relatively scarce. Some steps in that direction, with mixed success, were taken in the 1990s [17–21], and here we use TDDFT in the interaction of atoms with short-wavelength FEL radiation. TDDFT was previously thought to fail to describe strong-field ionization under IR radiation, because it had had limited success in accounting for the so-called knee in helium double ionization [12,22,23]. Instead, as discussed in the sections that follow, we find that TDDFT actually does provide a surprisingly good description of several aspects of the nonlinear dynamics of atoms driven by strong soft x-ray radiation. The remaining discrepancies between LOPT and TDDFT provide a road map towards further improvement, in preparation for the extension of the approach to shorter wavelengths and/or more complex systems.

In Sec. II we briefly present the theoretical methodology to study the ionization of Ne and Ar. We first introduce in Sec. II A the theoretical approach that we have used to calculate the ionization yields. We then show in Sec. II B how we model the laser field that we apply to our atoms. In Sec. II C we show how we obtain both the total and individual yields. Finally, in Sec. II D, we provide numerical details of how we perform the calculations and the reader can refer to the Appendix for more details. In Sec. III we present the results and discussion for the total and individual yields obtained for Ar and Ne atoms exposed to a strong-field, short-wavelength (soft x-ray) laser, as a function of the laser intensity. This is followed by concluding remarks in Sec. IV.

II. THEORETICAL BACKGROUND

A. Time-dependent density-functional theory

The central tenet of TDDFT is that all physical properties of an interacting many-electron system can be determined from its time-dependent density [24]. As in static DFT [25],

the interacting system is mapped—in principle exactly—onto an auxiliary, noninteracting system, the so-called Kohn-Sham (KS) system, which by construction yields the same time-dependent density as the interacting one. In the present work we are interested in the nonlinear dynamics of closed-shell electronic systems, and for N_0 electrons the density of the KS system is $n(\mathbf{r},t) = 2\sum_{i=1}^{N_0/2} |\phi_i(\mathbf{r},t)|^2$ (we here assume a spinless ground state), where $\phi_i(\mathbf{r},t)$ are single-particle KS orbitals satisfying the time-dependent KS (TDKS) equations (in atomic units):

$$i\frac{\partial}{\partial t}\phi_i(\mathbf{r},t) = \left[-\frac{\nabla^2}{2} + V_0(\mathbf{r}) + V_{\text{FEL}}(\mathbf{r},t) + V_{\text{H}}[n](\mathbf{r},t) \right. $$
$$\left. + V_{\text{xc}}[n](\mathbf{r},t) \right]\phi_i(\mathbf{r},t), \quad i = 1,\ldots,N_0/2. \quad (1)$$

Here $V_0(\mathbf{r})$ is the electrostatic potential of the nuclei, $V_{\text{FEL}}(\mathbf{r},t)$ describes the laser field, $V_{\text{H}}[n](\mathbf{r},t)$ is the Hartree potential, and $V_{\text{xc}}[n](\mathbf{r},t)$ is the exchange-correlation (xc) potential. In this work we consider different xc potential approximations: the local-density approximation [26] (LDA), PBE [27], and LB94 [28] forms of the generalized gradient approximations, and the corrected-exchange-density [29] extension of LDA (CXD-LDA). Further, we employ the adiabatic extension of these functionals to the time-dependent case.

B. Laser field

We model the laser-atom interaction within the dipole approximation using an external potential defined as

$$V_{\text{FEL}}(t) = Af(t)\sin(\omega t)\mathbf{r}\cdot\boldsymbol{\alpha}, \quad (2)$$

where $\boldsymbol{\alpha}$ is the polarization, ω the frequency, and A the field amplitude of the laser. This approximation is well justified under FEL experimental conditions. The pulse envelope is of Gaussian shape $f(t) = \exp[-(t-t_0)^2/2\tau_0^2]$, with the peak value centered at t_0 and the Full Width at Half Maximum (FWHM) intensity given by $2\sqrt{\ln 2}\,\tau_0$. A deterministic temporal shape as defined in Eq. (2) represents a simplified model compared to current FEL sources which, in general, exhibit strong intensity fluctuations.

C. Total and individual yields

To estimate the total ionic yields, we follow the time evolution of the charge remaining in a given volume V around the atom. The norm of each KS orbital inside this volume $N_i(t) = \int_V d\mathbf{r}\,|\phi_i(\mathbf{r},t)|^2$ decreases in time during the application of a strong short-wavelength laser pulse. The total number of escaped electrons at time t is given by

$$N_{\text{esc}}(t) = N_0 - N(t), \quad (3)$$

where N_0 is the initial number of electrons and $N(t) = \sum_i N_i(t) = \int_V d\mathbf{r}\,n(\mathbf{r},t)$ is the total number of remaining electrons in the volume at the given time. The total ionization yield is the long time limit of Eq. (3): $N_{\text{esc}} = N_{\text{esc}}(t \to \infty)$.

To calculate the individual ionization probabilities $P^{q+}(t)$ for an atom, i.e., the probability to produce an ion in a positively q-charged state ($q = 1,\ldots,N_0$), we employ the approach based on the time-dependent KS orbitals described in Ref. [30]. In this approximation, the ionization probability is defined as

the sum over all the combinations of KS probabilities $N_i(t)$ composing a q-charged state

$$P^{q+}(t) = \sum_{\sigma \in \mathbf{C}(N_0,q)} N_{\sigma(1)}(t) \cdots N_{\sigma(N-q)}(t), \qquad (4)$$

where $\mathbf{C}(N_0,q)$ is the set of all the possible configurations σ in which an $(N_0 - q)$-tuple can be selected from a $(1, \ldots, N_0)$ one. The total ionization yield can be reconstructed by computing a weighted sum over the different ionization channels. From LOPT we directly obtain all the individual ionic yields P^{q+} [10,11] and the total yield can be obtained with the same prescription. Within TDDFT, we can directly obtain the total yield either by summing up the individual ionization channels or by monitoring the total charge. In either case, the total yield is the only quantity that is rigorously correct since it can be directly derived from the total density. To obtain the individual ionic channels, we need to assume that the KS wave function is a good representation of the exact many-body one. The validity of this assumption in the present context has to be evaluated on the basis of its success in recapturing results from different approaches and, of course, experimental data.

D. Numerical details

In the following we present results for strong-field ionization of Ne and Ar atoms. We numerically propagate the TDKS equations (1) in real time and real space using the OCTOPUS code [31–33]. To this end we perform calculations in a 16 Å radius spherical box and discretize the problem on a Cartesian grid with spacing 0.16 Å. An 8 Å thick boundary absorber [34] is introduced to account for electrons escaping from the simulation box, which therefore acts as an integration volume V. Core excitations are expected to play a relevant role for intensities much higher than the ones considered in this paper [10,11]. For this reason we freeze the core electrons into a pseudopotential using the Troullier-Martins scheme [35] for both atoms: $1s$ electrons for Ne and $1s$, $2s$, and $2p$ electrons for Ar [36]. We refer the reader to the Appendix for more information regarding an assessment of the pseudopotential, the grid parameters, and the absorbing boundary used here.

III. RESULTS AND DISCUSSION

A. Ne atom

In Fig. 1 we compare TDDFT and LOPT total ionization yields for Ne as a function of the laser intensity, as depicted schematically in the inset. Here, the photon energy is fixed to $\omega = 93$ eV and we consider the cases of a short 5 fs FWHM (a) and a long 30 fs FWHM laser pulse (b). In the two cases we propagate in time the TDDFT equations for 25 and 153 fs, respectively. We then use an exponential fit near the end of the propagation to extrapolate the total ionization yield. The overall agreement is remarkably good for all the xc functionals in a wide range of intensities (plots are in log scale). However, as the intensity increases, the agreement gradually deteriorates with TDDFT tending towards lower ionization yields. This behavior is more pronounced in the 30 fs case in Fig. 1(b), where the TDDFT ion yield flattens out for intensities $\gtrsim 10^{15}$ W/cm^2, while the LOPT yields higher values. The observed deviation may trace back to
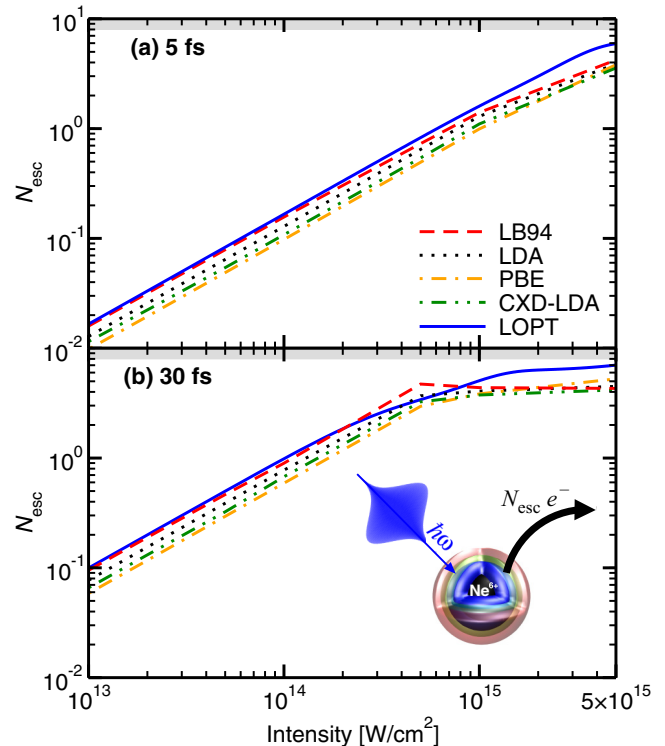

FIG. 1. (Color online) Ne total number of escaped electrons N_{esc} for different laser intensities and (a) 5 fs and (b) 30 fs FWHM pulses of $\omega = 93$ eV. Different TDDFT functionals are compared with LOPT. The Ne ionization process is shown as an inset. Shaded regions indicate the electrons frozen in the pseudopotential.

an improper time dependence of the xc potential for highly ionized species, as has been proven in one dimension for He, a two-electron system [37–39]. These effects become more severe for high intensities and build up for longer times because more electrons are ejected and the density changes are more substantial. For systems with more electrons we expect them to introduce some additional dynamical screening that can change the magnitude of these effects but not their presence. Consequently, there are spurious oscillations in the successive KS ionization potentials leading to increasing errors as the system loses electrons (see below). An error $\lesssim 10\%$ in the KS ionization potentials brought in by the pseudopotential for the strongly charged ions cannot alone justify the observed effect.

Because LOPT has shown itself to be in excellent agreement with experiment [8–11], we deduce that our TDDFT results have a tendency to slightly underestimate the total ionic yield. It must be added, however, that these differences are minor and are likely to fall within the present experimental accuracy of many FEL experiments. Therefore, we conclude that TDDFT has predictive power over a wide range of laser pulse intensities.

Not all the xc functionals perform in the same way. A characterizing property of both LB94 and CXD-LDA is the correct asymptotic tail decay $V_{xc} \sim -1/r$ following the Coulomb potential for large r. In contrast, both LDA and PBE decay exponentially. The high-lying unoccupied KS bound states, close to the ionization threshold, are thus expected to be more accurately described by the LB94 and CXD-LDA functionals.
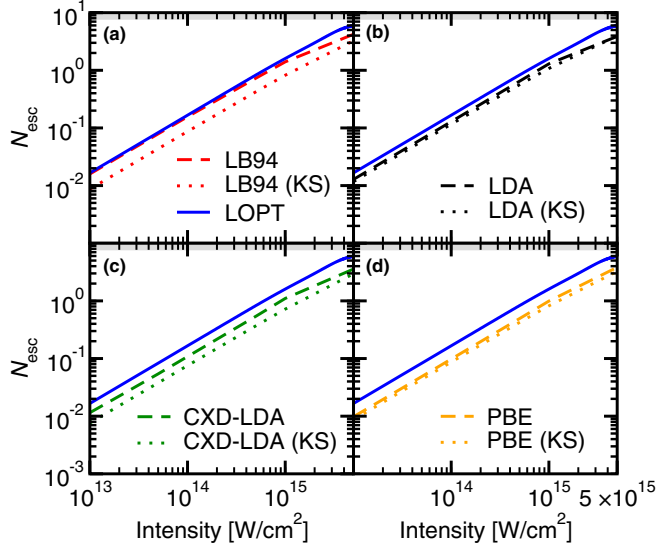
FIG. 2. (Color online) As in Fig. 1, but for a 5 fs FWHM pulse and different approximation levels: LB94, LDA, CXD-LDA, and PBE. In each panel we compare LOPT (solid), TDDFT (dashed), and the independent KS response (dotted). Shaded regions indicate the electrons included in the pseudopotential.
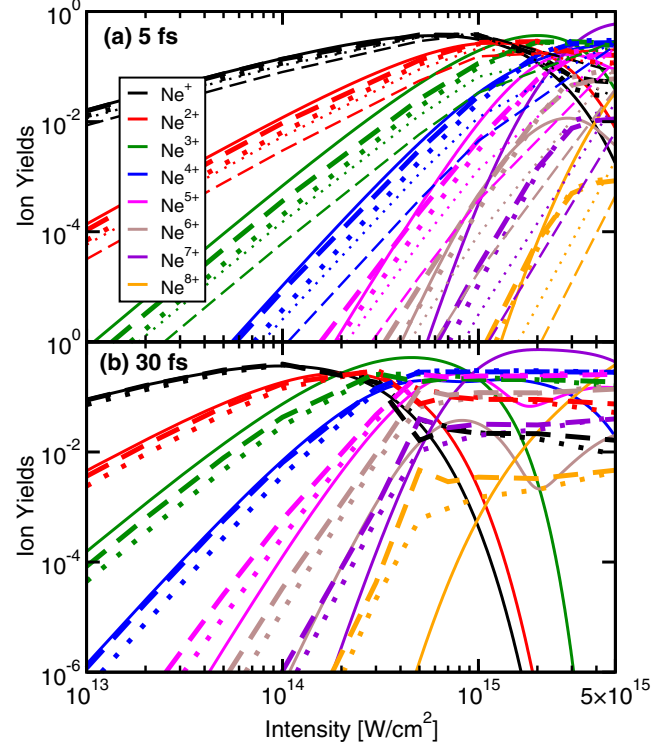

FIG. 3. (Color online) Ne individual ionization yields as a function of the intensity for 5 fs and 30 fs FWHM laser pulses of $\omega = 93$ eV. TDDFT (thicker) and the independent KS response (thinner) with LB94 (dashed) and LDA (dotted) functionals are compared to LOPT (solid). The individual channels are sorted in increasing order from left to right according to their charge status.

This is reflected in a superior description of the ionization process with LB94, since it provides the best agreement with LOPT. In this respect, the relatively poor accuracy of CXD-LDA compared to LB94 deserves further examination.

To discern the impact of the underlying ground state and the quality of the Hartree plus exchange-correlation functional, we compare in Fig. 2 the full solution of the TDKS with the one in which we keep V_H and V_{xc} frozen in the initial ground-state configuration (the independent KS response). Electrons are thus treated as noninteracting particles moving in a fixed external potential. The effects of such a crude approximation are almost indiscernible when the xc potential is short ranged, i.e., $V_{xc} \sim e^{-r}$, as for LDA and PBE [cf. Figs. 2(b) and 2(d)]. However, this is not the case when the xc potential is long ranged, i.e., $V_{xc} \sim -1/r$, as for LB94 and CXD-LDA [cf. Figs. 2(a) and 2(c)].

In an independent KS response picture, the total ionization yields are directly related to the KS eigenvalues. For long-ranged xc potentials, the KS eigenvalues are more strongly bound, reducing total ionization yields compared to short-ranged xc potentials. When the xc potential is propagated in time, ejected electrons may induce an attractive potential via redistribution of the electronic density on the ion. Thus, the kinetic energy of the ejected electrons will be reduced due to this stabilization of the electronic levels. To support our analysis we have employed linear response TDDFT to calculate the cross sections. From the Appendix, we see that the cross sections increase as the kinetic energies decrease below 93 eV [40], so we obtain a larger number of escaped electrons than when the xc potential is frozen. This effect becomes relevant mostly when the long-range electron-electron interaction is accurately described. This leads to a substantial modification in the number of electrons being ejected (~100% increase for LB94 and ~33% for CXD-LDA at $I = 10^{14}$ W/cm²).

In Fig. 3 we analyze Ne individual TDDFT (thicker) and the independent KS response (thinner) ionization yields obtained with LB94 and LDA using Eq. (4). We observe that the TDDFT ionic yields up to Ne⁴⁺ are in good agreement with those of LOPT for a large range of laser intensities: $I \lesssim 10^{15}$ W/cm² for a 5 fs pulse [Fig. 3(a)] and $I \lesssim 5 \times 10^{14}$ W/cm² for a 30 fs one [Fig. 3(b)]. For more strongly ionized species, Ne⁵⁺ through Ne⁸⁺, the discrepancy is larger, especially for the 30 fs pulse. From Fig. 3(a) we see that the individual ionization yields for all channels are ordered as LB94(KS) < LDA(KS) ~ LDA < LB94, as was also the case for the total ionization yields shown in Figs. 2(a) and 2(b).

The time locality of the xc potential introduces fluctuations that are amplified by the charge status of the ion [39]. As a consequence, the total and partial ionization yields are in good agreement with LOPT, as long as the channels with a charge status ⩾Ne⁵⁺ play a negligible role in the ionization process (cf. Figs. 1 and 3). Experimental ionization channels up to Ne⁶⁺ present excellent agreement with LOPT [8–11]. We can therefore conclude that TDDFT describes well the ionic yields up to Ne⁴⁺ with the current state-of-the-art experimental data.

The trend observed in the TDDFT total yields for the different xc functionals (Fig. 1) is reflected in the single ionization channels for both pulse lengths; namely, the inclusion of a correct asymptotic decay systematically improves the description of each channel.
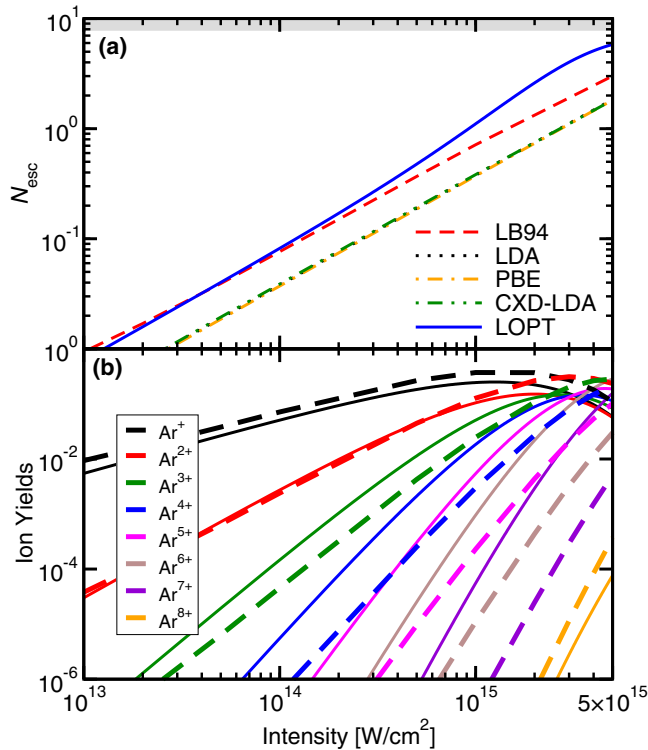
FIG. 4. (Color online) Ar total and individual ionic yields as a function of the laser intensity for a 10 fs FWHM laser pulse of $\omega = 105$ eV. (a) Total ionization yield for different TDDFT functionals and LOPT. (b) Individual ionization channels for LB94 (dashed) and LOPT (solid). The individual channels are sorted in increasing order from left to right according to their charge status. The Ar ionization process is shown as an inset. Shaded regions indicate electrons frozen in the pseudopotential.

B. Ar atom

In Fig. 4 we present the results for total and individual ionization yields of Ar, as depicted schematically in the inset, for a 10 fs FWHM pulse of energy $\omega = 105$ eV and a full propagation time of 51 fs. The total ionization yields for all the considered functionals except LB94, [Fig. 4 (b)], qualitatively follow LOPT but systematically predict lower values. LB94 remarkably reproduces LOPT up to $I \lesssim 5 \times 10^{14}$ W/cm^2. For higher intensities, it departs towards lower ionization values similarly to what was observed for Ne in Fig. 1. The intensity dependence of single ionization channels, as shown in Fig. 4(b), is in good agreement up to Ar^{3+} for LB94 only. It then quickly deteriorates for higher ionized species.

From experimental results [16] we know that when the Ar^{6+} is produced, it is composed of an ionized small contribution and a much larger contribution on an excited state. However, its ionized contribution is the predominant one to produce Ar^{7+} and Ar^{8+}. Additionally, the single ionization contribution to Ar^{7+} is also much larger than the double ionization contribution to Ar^{8+}. The strongly ionized Ar^{7+} is here produced through a sequential ionization process involving a shakeup step where a photon ejects one electron in the continuum while leaving the parent ion in an excited state [16]. Discarding this ionization pathway in LOPT leads to an Ar^{7+} yield reduced up to a factor of 4 orders of magnitude with respect to experiment.

In general, TDDFT tends to underestimate the LOPT results for highly charged channels. The shakeup experimental effect for Ar^{7+} is only partially accounted for in TDDFT, since none of the xc functionals we employed are self-interaction free. On the other hand, for Ne^{8+} and Ar^{8+}, spurious correlation effects between the core electrons frozen in the pseudopotential and the escaped electrons in the absorbing boundary are included. This may lead to the overestimation of TDDFT with respect to LOPT. For this reason, in TDDFT the Ar^{7+} channel is strongly suppressed, while the Ar^{8+} channel is strongly enhanced. However, as we are most interested in the intensity regime where LOPT is expected to be valid, these issues are not so relevant for this study.

IV. CONCLUSIONS

In conclusion, we have compared TDDFT and LOPT ionization yields for Ar and Ne subjected to intense soft x-ray radiation. Overall, for both short and long pulse durations, TDDFT results display noteworthy similarities with LOPT results throughout a wide range of intensities and within present-day experimental error. Using a functional with the correct asymptotic behavior significantly improves the potential applicability of TDDFT. Since the two approaches are built on completely different bases, the resulting agreement indicates that both are able to provide a realistic picture of the underlying physics. In particular, this work results in the demonstration of an unexpected predictive power of TDDFT in describing total and individual ionization yields in FEL experiments. We believe that, in addition to the illustration of the predictive potential of TDDFT in the present context, this work introduces a road map for the exploration of nonperturbative approaches in short-wavelength strong-field physics, with a number of open questions to be addressed.

APPENDIX: ASSESSMENT OF THE PSEUDOPOTENTIAL, GRID PARAMETERS, AND ABSORBING BOUNDARY

1. Absorbing boundaries and continuum states description

Modeling ionization processes involves a minute description of the interaction (through a laser pulse) between bound and continuum states. A description of finite-volume continuum states in real-space real-time propagation methods is customarily achieved through the use of boundary absorbers

[34]. In the absence of such absorbers, the electronic wave packets are reflected back and forth at the boundaries of the simulation box. Complex absorbing potentials (CAPs) constitute a widely used solution to eliminate such reflections [41,42]. We implement our boundary condition by inserting into the system's Hamiltonian an additional (spherically symmetric) imaginary potential $V_{CAP}(r)$ acting at a certain distance R_{CAP} from the center of the box of radius R,

$$V_{CAP}(r) = -i\eta \begin{cases} 0 & \text{if } r < R_{CAP}, \\ \sin^2\left(\frac{\pi(r-R_{CAP})}{2(R-R_{CAP})}\right) & \text{if } R_{CAP} \leqslant r \leqslant R. \end{cases}$$
(A1)

Time propagation with a Hamiltonian containing V_{CAP} enforces a wave-function damping in the region near the edges of the simulation box. The absorption properties of this CAP as a function of the outgoing electron's kinetic energy depends on the values of η and R_{CAP}.

We find that for a spherical box of radius $R = 16$ Å, a CAP having $\eta = 1$ and $R_{CAP} = 8$ Å is enough to guarantee good continuum properties in the outgoing electron's kinetic energy range that we consider in this work for Ne and Ar. To check this we have compared the experimental absorption spectra to the one obtained from TDDFT for different absorbing boxes until reflections are negligible for this range.

To assess the quality of the present choice, in Figs. 5 and 6 we show Ne and Ar absorption cross sections σ obtained with different xc functionals for energies in the continuum, above the first ionization threshold. These cross sections have been calculated in the linear regime analyzing the time evolution of the atomic dipole moment [44].

For both Ne and Ar, the cross-section presents spurious oscillations reminiscent of box states for energies $\lesssim 20$ eV above the ionization threshold. For larger values our CAP is well absorbing and the cross sections smoothly follow the experimental ones [43].

FIG. 6. (Color online) Same as in Fig. 5, but for the Ar absorption cross section. In the inset we focus on the range of energies relevant for ionization from a $\omega = 105$ eV laser pulse.

If we discard nonlinear effects, the kinetic energy of an electron ejected by an ionizing laser pulse is given by $E = I_p - \omega$, where I_p is the ionization potential of the bound electron and ω the laser energy. Under the assumption that the energy absorbed from the laser is integrally transformed into the kinetic energy of the escaping electron, we can conclude that the absorption cross section in the continuum is proportional to the electron photoemission probability. The I_p in TDDFT is given by the KS eigenvalue of each bound electron. A rough estimate of the TDDFT quality attained in the description of ionization processes initiated by a laser of a given frequency ω is therefore given by the behavior of σ in an energy range identified by the deeper and higher KS ionization potentials. In the insets of Figs. 5 and 6 we plot σ in the energy range relevant for a laser of $\omega = 93$ eV (Ne) and $\omega = 105$ eV (Ar), respectively. We can therefore conclude that in the energy range associated with our pulses, there are no spurious reflections and the absorption cross sections agree remarkably with the experimental ones.

2. Pseudopotential accuracy

In Table I, we show the relative percentage errors introduced by the pseudopotential in the outermost valence energy levels of Ar and Ne for increasing ionized species and the different xc functionals tested. The error is here evaluated relative to an all-electron calculation. Since our pseudopotentials have been generated from a neutral ground-state configuration, the errors increase linearly as a function of the charged state. Here the errors are larger for Ne than for Ar, because Ne pseudopotentials have been generated using a larger radial cutoff. The spacing of 0.16 Å we have used is small enough to describe accurately the steep Coulomb potential for the innermost core eigenvalues with charge $+6$ and $+7$. The eigenvalue errors for all the functionals are between 0.001 and 0.01 Ha.
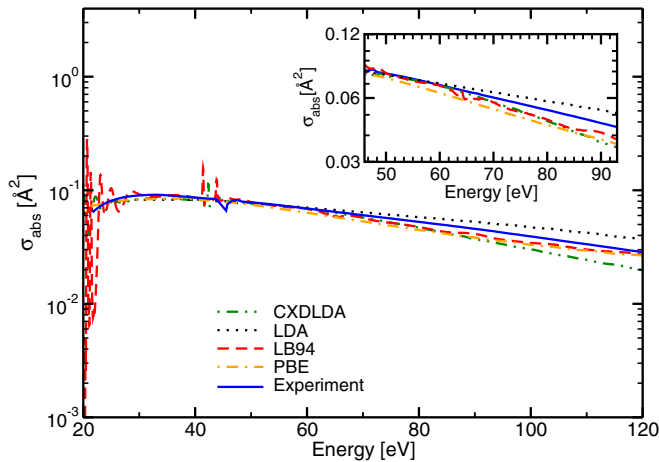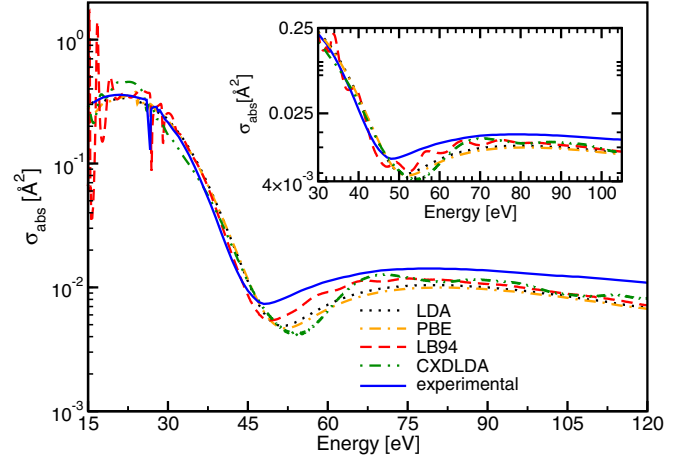

FIG. 5. (Color online) Ne absorption cross section (logarithmic scale) above the first ionization threshold. Result for different TDDFT xc functionals (LDA, PBE, CXD-LDA, and LB94) compared with experimental data [43]. In the inset we focus on the range of energies relevant for ionization from a $\omega = 93$ eV laser pulse.

TABLE I. Ne and Ar pseudopotential vs all-electron relative percentage errors for the outermost valence states for different xc functionals.

Functional/ Rel. err. (%)	Ne^+ / Ar^+	Ne^{2+} / Ar^{2+}	Ne^{3+} / Ar^{3+}	Ne^{4+} / Ar^{4+}	Ne^{5+} / Ar^{5+}	Ne^{6+} / Ar^{6+}	Ne^{7+} / Ar^{7+}
LDA							
$2s$ / $3s$	−0.39 / 0.04	−0.41 / 0.10	−0.11 / 0.20	0.42 / 0.32	1.13 / 0.49	1.97 / 0.73	1.39 / 1.10
$2p$ / $3p$	0.18 / 0.06	0.99 / 0.14	2.20 / 0.25	3.68 / 0.41	5.31 / 0.61	7.05 / 0.91	7.18 / 1.35
$3d$ / $3d$	−0.07 / 0.08	0.33 / 0.21	1.93 / 0.37	4.12 / 0.59	6.47 / 0.89	8.82 / 1.33	10.10 / 2.02
PBE							
$2s$ / $3s$	−0.42 / 0.03	−0.47 / 0.06	−0.18 / 0.12	0.35 / 0.18	1.05 / 0.27	1.91 / 0.40	1.21 / 0.72
$2p$ / $3p$	0.16 / 0.04	0.98 / 0.10	2.21 / 0.17	3.69 / 0.26	5.35 / 0.39	7.21 / 0.59	7.40 / 0.97
$3d$ / $3d$	−0.08 / 0.08	0.30 / 0.18	1.85 / 0.31	3.99 / 0.48	6.32 / 0.72	8.73 / 1.09	10.03 / 1.75
LB94							
$2s$ / $3s$	−0.19 / 0.10	−0.03 / 0.27	0.39 / 0.51	0.99 / 0.85	1.60 / 1.33	1.96 / 2.04	1.88 / 3.26
$2p$ / $3p$	0.34 / 0.12	1.22 / 0.30	2.48 / 0.58	3.99 / 0.96	5.61 / 1.49	7.16 / 2.28	8.11 / 3.63
$3d$ / $3d$	−0.10 / 0.08	0.47 / 0.35	1.79 / 0.74	3.58 / 1.28	5.56 / 2.04	7.58 / 3.11	8.87 / 4.93
CXD-LDA							
$2s$ / $3s$	−0.21 / 0.07	−0.41 / 0.10	0.02 / 0.06	0.59 / 0.16	1.28 / 0.53	1.89 / 0.60	1.71 / 1.65
$2p$ / $3p$	0.35 / 0.09	0.84 / 0.14	2.15 / 0.09	3.61 / 0.22	5.19 / 0.65	6.67 / 0.75	7.33 / 1.91
$3d$ / $3d$	0.04 / 0.06	0.54 / 0.19	1.83 / 0.15	3.63 / 0.30	5.64 / 0.86	7.71 / 1.07	9.36 / 2.43

[1] P. Emma, R. Akre, J. Arthur, R. Bionta, C. Bostedt, J. Bozek, A. Brachmann, P. Bucksbaum, R. Coffee, F.-J. Decker, Y. Ding, D. Dowell, S. Edstrom, A. Fisher, J. Frisch, S. Gilevich, J. Hastings, G. Hays, P. Hering *et al.*, Nat. Photon. **4**, 641 (2010).

[2] W. Ackermann, G. Asova, V. Ayvazyan, A. Azima, N. Baboi, J. Bähr, V. Balandin, B. Beutner, A. Brandt, A. Bolzmann, R. Brinkmann, O. I. Brovko, M. Castellano, P. Castro, L. Catani, E. Chiadroni, S. Choroba, A. Cianchi, J. T. Costello *et al.*, Nat. Photon. **1**, 336 (2007).

[3] J. Feldhaus, M. Krikunova, M. Meyer, T. Möller, R. Moshammer, A. Rudenko, T. Tschentscher, and J. Ullrich, J. Phys. B: At. Mol. Opt. Phys. **46**, 164002 (2013).

[4] C. Bostedt, J. D. Bozek, P. H. Bucksbaum, R. N. Coffee, J. B. Hastings, Z. Huang, R. W. Lee, S. Schorb, J. N. Corlett, P. Denes, P. Emma, R. W. Falcone, R. W. Schoenlein, G. Doumy, E. P. Kanter, B. Kraessig, S. Southworth, L. Young, L. Fang *et al.*, J. Phys. B: At. Mol. Opt. Phys. **46**, 164003 (2013).

[5] A. A. Sorokin, S. V. Bobashev, T. Feigl, K. Tiedtke, H. Wabnitz, and M. Richter, Phys. Rev. Lett. **99**, 213002 (2007).

[6] M. Richter, S. V. Bobashev, A. A. Sorokin, K. Tiedtke, J. Phys. B: At. Mol. Opt. Phys. **43**, 194005 (2010).

[7] M. G. Makris, P. Lambropoulos, and A. Mihelic, Phys. Rev. Lett. **102**, 033002 (2009).

[8] P. Lambropoulos, K. G. Papamihail, and P. Decleva, J. Phys. B: At. Mol. Opt. Phys. **44**, 175402 (2011).

[9] P. Lambropoulos and G. M. Nikolopoulos, Eur. Phys. J. Spec. Top. **222**, 2067 (2013).

[10] P. Lambropoulos, G. M. Nikolopoulos, and K. G. Papamihail, Phys. Rev. A **83**, 021407(R) (2011).

[11] G. M. Nikolopoulos and P. Lambropoulos, J. Phys. B: At. Mol. Opt. Phys. **47**, 115001 (2014).

[12] P. Lambropoulos, P. Maragakis, and J. Zhang, Phys. Rep. **305**, 203 (1998).

[13] B. Rudek, S.-K. Son, L. Foucar, S. W. Epp, B. Erk, R. Hartmann, M. Adolph, R. Andritschke, A. Aquila, N. Berrah, C. Bostedt, J. Bozek, N. Coppola, F. Filsinger, H. Gorke, T. Gorkhover, H. Graafsma, L. Gumprecht, A. Hartmann *et al.*, Nat. Photon. **6**, 858 (2012).

[14] A. S. Simonsen, S. A. Sørngård, R. Nepstad, and M. Førre, Phys. Rev. A **85**, 063404 (2012).

[15] L. Malegat, H. Bachau, B. Piraux, and F. Reynal, J. Phys. B: Mol. Opt. Phys. **45**, 175601 (2012).

[16] M. Ilchen *et al.* (private communication).

[17] C. A. Ullrich, U. J. Gossmann, and E. K. U. Gross, Ber. Bunsenges. Phys. Chem. **99**, 488 (1995).

[18] C. A. Ullrich and E. K. U. Gross, Comments At. Mol. Phys. **33**, 211 (1997).

[19] X.-M. Tong and Shih-I. Chu, Phys. Rev. A **57**, 452 (1998).

[20] D. G. Lappas and R. van Leeuwen, J. Phys. B: At. Mol. Opt. Phys. **31**, L249 (1998).

[21] M. Lein, E. K. U. Gross, and V. Engel, Phys. Rev. Lett. **85**, 4707 (2000).

[22] M. Petersilka and E. K. U. Gross, Laser Phys. **9**, 105 (1999).

[23] D. Bauer and F. Ceccherini, Opt. Express **8**, 377 (2001).

[24] E. Runge and E. K. U. Gross, Phys. Rev. Lett **52**, 997 (1984).

[25] W. Kohn and L. J. Sham, Phys. Rev. **140**, A1133 (1965).

[26] J. P. Perdew and Y. Wang, Phys. Rev. B **45**, 13244 (1992).

[27] J. P. Perdew, K. Burke, and M. Ernzerhof, Phys. Rev. Lett. **77**, 3865 (1996).

[28] R. van Leeuwen and E. J. Baerends, Phys. Rev. A **49**, 2421 (1994).

[29] X. Andrade and A. Aspuru-Guzik, Phys. Rev. Lett. **107**, 183002 (2011).

[30] C. A. Ullrich, J. Mol. Struct.: THEOCHEM **501-502**, 315 (2000).

[31] M. A. L. Marques, A. Castro, G. F. Bertsch and A. Rubio, Comput. Phys. Commun. **151**, 60 (2003).

[32] A. Castro, M. A. L. Marques, H. Appel, M. Oliveira, C. A. Rozzi, X. Andrade, F. Lorenzen, E. K. U Gross and A. Rubio, Phys. Stat. Sol. B **243**, 2465 (2006).

[33] X. Andrade, J. Alberdi-Rodriguez, D. A. Strubbe, M. J. T. Oliveira, F. Nogueira, A. Castro, J. Muguerza, A. Arruabarrena,

S. G. Louie, A. Aspuru-Guzik, A. Rubio, and M. A. L. Marques, J. Phys.: Condens. Matter **24**, 233202 (2012).

[34] U. De Giovannini, A. H. Larsen, and A. Rubio, (unpublished).

[35] N. Troullier and J. L. Martins, Phys. Rev. B **43**, 1993 (1991).

[36] M. Oliveira and F. Nogueira, Comput. Phys. Commun. **178**, 524 (2008).

[37] J. I. Fuks, N. Helbig, I. V. Tokatly, and A. Rubio, Phys. Rev. B **84**, 075107 (2011).

[38] J. I. Fuks, P. Elliott, A. Rubio, and N. T. Maitra, J. Phys. Chem. Lett. **4**, 735 (2013).

[39] P. Elliott, J. I. Fuks, A. Rubio, and N. T. Maitra, Phys. Rev. Lett. **109**, 266404 (2012).

[40] X.-M. Tong and Shih-I. Chu, Phys. Rev. A **55**, 3406 (1997).

[41] C. Leforestier and R. E. Wyatt, J. Chem. Phys. **78**, 2334 (1983).

[42] R. Kosloff and D. Kosloff, J. Comput. Phys. **63**, 363 (1986).

[43] J. A. R. Samson and W. C. Stolte, J. Electron Spectrosc. **123**, 265 (2002).

[44] M. A. L. Marques, N. T. Maitra, F. Nogueira, E. K. U. Gross, and A. Rubio, *Fundamentals of Time-Dependent Density Functional Theory*, Lecture Notes in Physics, Vol. 837 (Springer, Berlin, 2011).